NANO LETTERS

pubs.acs.org/NanoLett

Letter

Tunable Magnetic Domains in Ferrimagnetic $MnSb_2Te_4$

Tatiana A. Webb, Afrin N. Tamanna, Xiaxin Ding, Nishchhal Verma, Jikai Xu, Lia Krusin-Elbaum,* Cory R. Dean,* Dmitri N. Basov,* and Abhay N. Pasupathy*

Cite This: *Nano Lett.* 2024, 24, 4393−4399

Read Online

ACCESS | Metrics & More | Article Recommendations | Supporting Information

ABSTRACT: Highly tunable properties make $Mn(Bi,Sb)_2Te_4$ a rich playground for exploring the interplay between band topology and magnetism: On one end, $MnBi_2Te_4$ is an antiferromagnetic topological insulator, while the magnetic structure of $MnSb_2Te_4$ (MST) can be tuned between antiferromagnetic and ferrimagnetic. Motivated to control electronic properties through real-space magnetic textures, we use magnetic force microscopy (MFM) to image the domains of ferrimagnetic MST. We find that magnetic field tunes between stripe and bubble domain morphologies, raising the possibility of topological spin textures. Moreover, we combine *in situ* transport with domain manipulation and imaging to both write MST device properties and directly measure the scaling of the Hall response with the domain area. This work demonstrates measurement of the local anomalous Hall response using MFM and opens the door to reconfigurable domain-based devices in the M(B,S)T family.

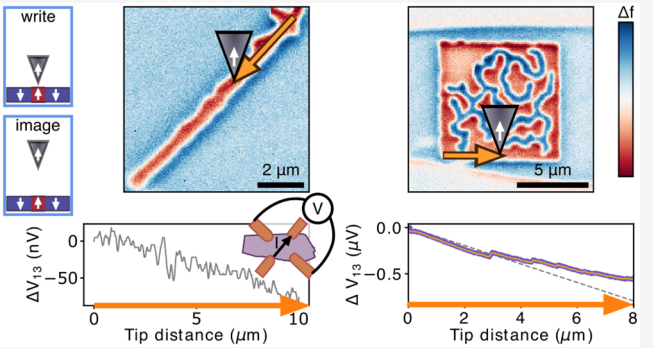

KEYWORDS: *magnetic topological materials, magnetic force microscopy, anomalous Hall effect, 2D materials, magnetic domains*

The recent discovery of $MnBi_2Te_4$ (MBT)[1−5] was a breakthrough to realize the quantum anomalous Hall effect in a stoichiometric crystal, avoiding the need for disorder-inducing magnetic dopants.[6−9] In addition, crystals are exfoliatable down to few layer thicknesses enabling integration into Van der Waals heterostructures with well developed fabrication techniques.[1,10−12] This discovery was rapidly followed by work extending MBT into a family of materials with highly tunable properties via crystallographic and chemical paradigms.[4,5,13−21] Substituting Sb for Bi changes the doping from n-type to p-type.[16,22] However, surprisingly, within MST, the magnetic order can also be tuned (via the concentration of magnetic defects) from A-type antiferromagnetic seen in MBT, where planes of Mn moments are aligned ferromagnetically (antiferromagnetically) within the plane (between planes), to ferrimagnetic with net out of plane magnetization.[19,21,23−25] The ability to tune the effective interplane coupling from antiferromagnetic to ferromagnetic strongly suggests the presence of magnetic frustration in M(B,S)T, raising the possibility of stabilizing other interesting magnetic orders.[26,27]

The ability to tune magnetic order in the M(B,S)T family opens more conventional applications of magnetic materials, where intense efforts have gone into developing materials structures with interdependent magnetic and electronic properties for control of charge and spin transport (e.g., magnetic data storage and spintronics). Growing evidence suggests that, while there are multiple proposals for band topology of MST[3,16,19,22,28,29] (work from some of us finds ferrimagnetic MST to be a Weyl semimetal[30]), the low energy bands of MST are nonetheless sensitive to the details of magnetic order,[3,19,24,28,29,31] but we do not yet have a detailed understanding of the correlation between electronic properties and real-space magnetic textures in MST. So far, the use of magnetism to control electronic properties in magnetic topological materials has been explored primarily in terms of topological phase transitions (e.g., refs 10, 12, 31, and 32) and manipulating chiral edge modes of the quantum anomalous Hall effect.[11,33,34] Edge mode manipulation has been demonstrated via magnetic domains in Cr-doped $(Bi,Sb)_2Te_3$[33,34] and via layer-dependent magnetization in antiferromagnetic MBT.[11] In magnetic materials more generally, domain manipulation and control has long been demonstrated using a variety of techniques including electrical currents, magnetic field gradients, and local magnetic fields, e.g., refs 33−41. However, to the best of our knowledge, the ability to write arbitrary-shaped domains in ferrimagnetic M(B,S)T compounds has yet to be investigated. In this work, we therefore set out to investigate what magnetic textures can be realized in MST and the

Received: December 21, 2023
Revised: March 17, 2024
Accepted: March 18, 2024
Published: April 3, 2024

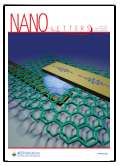

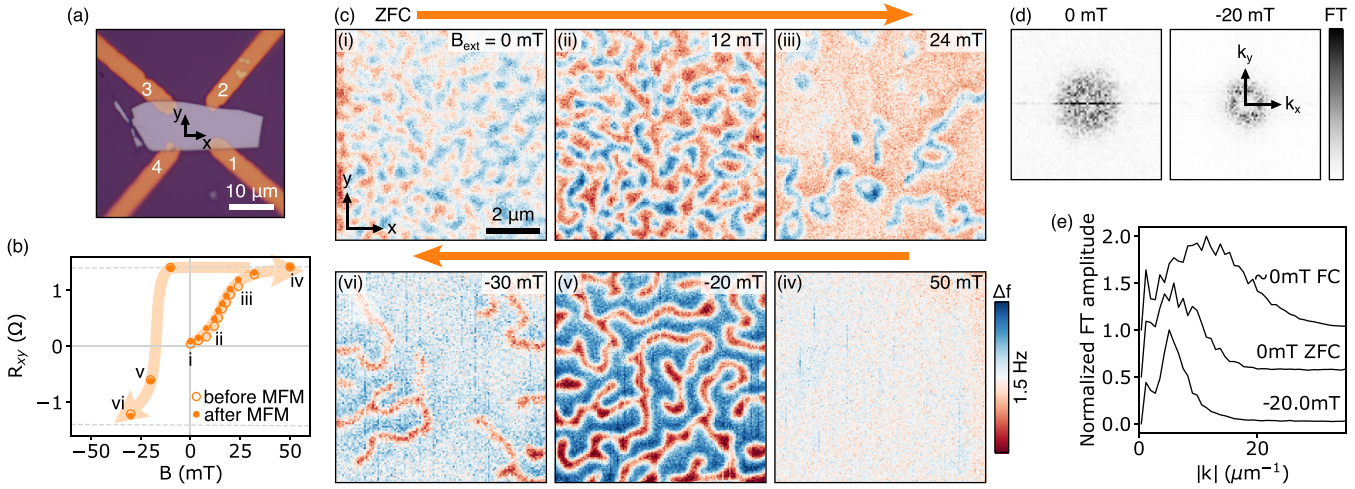

Figure 1. Evolution of stripe domains under B_{ext}. (a) Optical micrograph of the MST device showing the MST flake with 4 contacts for transport measurements in a Van der Pauw geometry. The arrows show the scan axes of the MFM images. (b) Magnetic field B_{ext} dependence of the Hall resistance R_{xy} measured at 5 K starting from a zero-field cool. Measurements were recorded before (open symbols) and after (filled symbols) MFM imaging. The light orange lines are guides to the eye, showing the order of data acquisition. (c) Constant height MFM measurements of the magnetic domains at the center of the MST device were recorded at 5 K after zero-field cooling. Measurements were interspersed with R_{xy} and R_{xx} measurements shown in (b) and in Supporting Information SIV. The arrows indicate the order of data acquisition. The color scale on all images is 1.5 Hz, but the zero values have been offset. The tip was lifted 300 nm above the SiO_2 surface. (d) Amplitude of the Fourier transforms of (c-i) and (c-v) after mean value subtraction. (e) Angular averaged amplitude of the Fourier transformed MFM data.

prospects for manipulating the local magnetization to create configurable devices. Specifically, we use the domain imaging and writing capabilities of magnetic force microscopy (MFM) combined with *in situ* transport to directly measure the device response to local changes in magnetization.

Our interdependent transport and magnetic measurements were performed on an exfoliated flake of ferrimagnetic MST (Figure 1a) with average thickness 84 nm and ±10 nm variations (Supporting Information SII). Four gold contacts were used to measure the longitudinal R_{xx} and Hall R_{xy} resistance. Immediately after device fabrication, R_{xx} showed a peak at 27 K on cooling, consistent with typical Curie temperatures seen in MST. At 2 K, the hysteretic loop in R_{xy} and peaks in R_{xx} as a function of the magnetic field showed a coercive field near 10 mT (Supporting Information SIV). Refer to Supporting Information SI for additional details on sample fabrication and characterization.

To characterize the magnetic domains in MST, we performed MFM in a cryogenic atomic force microscope (AFM) with a variable magnetic field B_{ext} normal to the sample surface. Figure 1c-i shows an MFM image of the zero-field cooled (ZFC) sample at 5 K. Because the coercive field of MST is so low, we quenched the superconducting magnet prior to cooling the sample to ensure a true ZFC with no trapped flux. The MFM image is a measurement of Δf, the resonance frequency shift of the AFM cantilever due to the interaction of the sample's stray fields with the cantilever's magnetic tip, so we expect images to primarily detect the domain structure of the ferromagnetically aligned components of MST's ferrimagnetic ordering.[42,43] Correspondingly, the ZFC image shows disordered maze-like stripe domains (Figure 1) consistent with ferromagnetic ordering in the out of plane direction, similar to domain images in bulk single crystals from Ge et al.[25] Applying magnetic field B_{ext} normal to the sample surface polarizes the sample (c-i to iv), increasing the area of the domains aligned with the field until, at 50 mT, only a single domain remains, giving a uniform MFM signal. *In situ* transport measurements show an associated increase in R_{xy} from 0.04 to 1.42 Ω. Over this range of B_{ext}, the contribution to R_{xy} from the linear Hall effect is negligible, so the change in R_{xy} is primarily due to the anomalous Hall effect (AHE)[44] (Supporting Information SVII).

Reversing the magnetic field (Figure 1c-iv to vi), we observe the reformation of stripe domains at −20 mT as R_{xy} drops and changes sign, indicating the reversal of the magnetization. These field-reversed domains are significantly less disordered than the ZFC domains. To quantify the difference, we examined the Fourier transforms (FTs) of the ZFC and −20 mT images, shown in Figure 1d. Both exhibit a ring shape, or a peak in the angular-averaged FT (Figure 1e), indicating the domains have a characteristic length scale, as expected from the energetics of domain formation.[45,46] The peak occurs at wavevector $|k| = 6.3\ \mu m^{-1}$ with standard deviation $\sigma = 4.8\ \mu m^{-1}$ for the ZFC domains and $|k| = 5.7\ \mu m^{-1}$ with $\sigma = 2.1\ \mu m^{-1}$ for the −20 mT domains. The broader peak associated with the ZFC domains indicates that, during cooling, the domains form features with a wider range of length scales compared to during magnetization reversal at low temperature.

To further explore how an external field can tune the domain morphology, we cooled the MST device from 35 K below T_c under $|B_{ext}|$ as large as 15 mT (Figure 2). With $|B_{ext}|$ larger than 10 mT, a single domain forms across the entire MST flake. However, when we nominally zero the magnet's current such that a small $B_{ext} \approx 0$ exists only from trapped flux, we see circular features in the MFM rather than stripe domains. MST is thus remarkably sensitive to small magnetic fields. As we discuss in Supporting Information SXII, without drawing conclusions about the mechanistic origin and the topology of the circular domains, we refer to these circular objects as bubble domains. At intermediate $|B_{ext}|$ (10 mT), the domains formed are not uniform in size and shape, and it is not clear whether they are intrinsically bubbles or stripes. We now focus on $B_{ext} \approx 0$, where bubbles are clearly observed.

The bubble domains are highly disordered (Figure 2e). The nearly isotropic Fourier transform (f) shows no evidence of

https://doi.org/10.1021/acs.nanolett.3c05058
Nano Lett. 2024, 24, 4393−4399

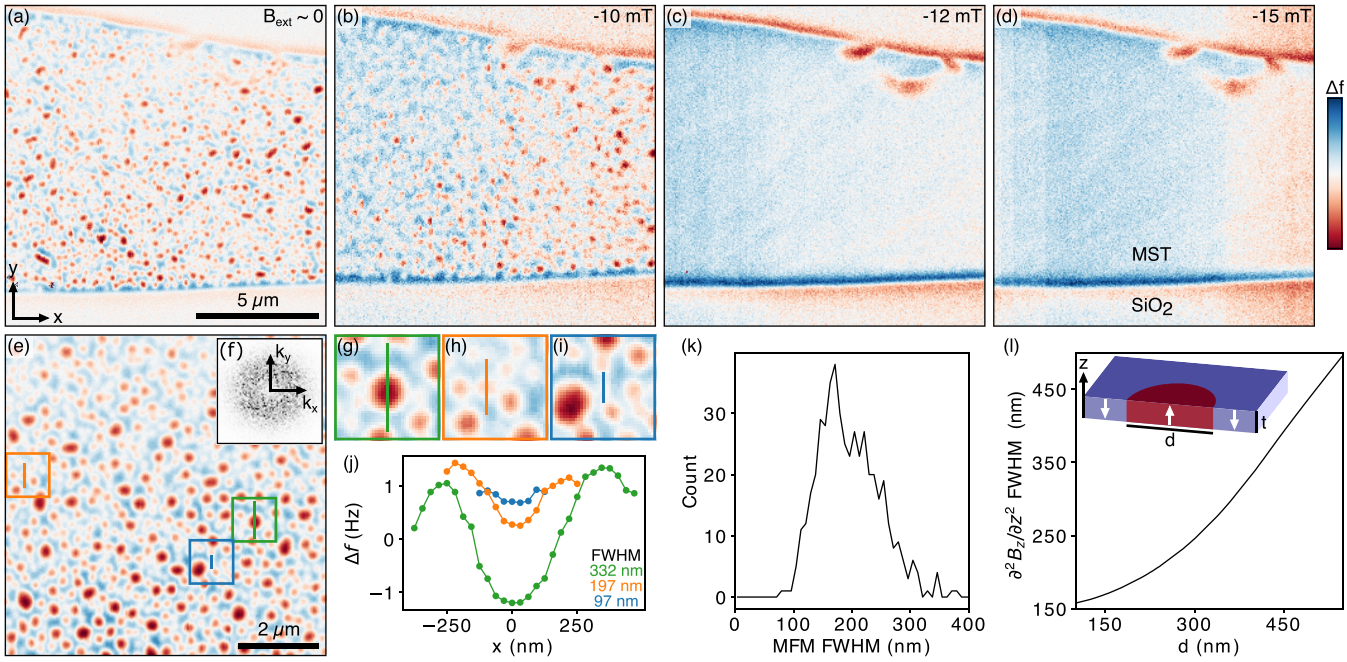

Figure 2. Field cooled domain structures. (a–d) Constant height MFM images of the magnetic domains in the MST device under field cooling with the indicated B_{ext}. The tip was lifted 300 nm above the SiO_2 surface. The range and offset of the color scale have been chosen for each image independently. Color scale range: 3.7 Hz (a), 1.5 Hz (b), 1.4 Hz (c), 1.5 Hz (d). Temperature: 5 K (a), 10 K (b–d). (a) $B_{ext} \sim 0$ indicates that a small unknown residual flux from the superconducting magnet was present. (e) Smaller scale constant height MFM image after cooling under $B_{ext} \sim 0$ showing clear bubble shaped domains. Color scale range: 4.4 Hz. Temperature: 5 K. The images in (a) and (e) are from separate cooling cycles with the same B_{ext}. (f) Amplitude of the Fourier transform of (e) after mean value subtraction. (g–i) Zooms of 3 regions in (e) showing a large, medium, and small size bubble. (j) Profiles through the large, medium, and small size bubbles from (g–i). (k) Histogram of the full-width-at-half-max (fwhm) of the bubbles imaged via MFM, determined from horizontal and vertical profiles through all resolvable bubbles in (e). The MFM fwhm is not directly interpretable as the bubble domain size. (l) fwhm of $\partial^2 B_z/\partial z^2$ for the stray magnetic field generated by a bubble domain with diameter d, using sample thickness t = 81.2 nm and z = 300 nm measured from the bottom of the material.

lattice organization, and the distribution of wavevectors centered at $|k| = 11.3\ \mu m^{-1}$ with $\sigma = 7\ \mu m^{-1}$ is extremely broad. Correspondingly, the circular MFM features range in size from below 100 nm to above 300 nm, as shown by the distribution of full width at half-maximum (fwhm) values (Figure 2k). The size of the features seen in MFM cannot directly be interpreted as the size of the domains in the MST. Approximating the tip as a point dipole with small oscillation amplitude, the MFM image Δf is proportional to $\partial^2 B_z/\partial z^2$ arising from the sample's stray field.[42,43] To help interpret the MFM features, we model the stray field for a single cylindrical bubble domain at a representative height z. As the domain diameter decreases below z, the spatial peak in $\partial^2 B_z/\partial z^2$ decreases in intensity (Supporting Information SV) and the fwhm saturates at a lower limit near 150 nm (Figure 2l). The fwhm does not decrease linearly in the domain diameter for small bubbles. The finite shape of the tip will cause additional smearing making features larger in the image than in $\partial^2 B_z/\partial z^2$, and the 150 nm cuttoff is an underestimate. Returning to the MFM data, we therefore expect small bubbles may not be detectable due to weak intensity, and for slightly larger bubbles, the apparent size in MFM may saturate at a lower limit larger than the domain diameter. The MFM data, however, show bubbles with fwhm below the expected 150 nm cutoff, likely because the width of the low intensity bubbles can be dominated by the positions of the neighboring bubbles. We therefore conclude that we observe bubbles down to the smallest sizes detectable in our MFM measurements, and so, there may be bubbles with sizes even smaller than represented in the histogram. Under repeat cooling, we find that some but not all bubbles form in the same location (Supporting Information SIX), which along with their disordered organization suggests preferred nucleation and pinning, either due to crystal inhomogeneity or extrinsic factors such as strain. While bubble domains may exist at the corners of the hysteresis loops at the nucleation or disappearance of the stripes,[47,48] a much higher bubble density is achieved on field cooling.

The above observations are consistent with the well-understood domain physics of thin ferromagnets with perpendicular magnetic anisotropy: (1) The sloped sides of the hysteresis loops correspond to stripe domain growth. (2) With sufficient magnetic anisotropy, a range of magnetic field can stabilize bubble domains, as a result of the competition between the domain wall and stray field energy costs. (3) Constraints including nucleation can impact disorder in the domain shapes.[45–47,49] Moreover, the observation of bubble domains raises the possibility of topologically nontrivial spin textures in MST. Chiral magnetic textures with similar phenomenology have been well studied in a variety of materials platforms with a Dyalozhinsky–Moriya interaction (DMI)[38,48,50–55] but also can be stabilized in materials without a DMI.[26,27,56] As we discuss in Supporting Information SXII, our data cannot determine the topology and potential chirality of the domains, which therefore remains an interesting avenue for future work.

So far, we have discussed how the domain morphology can be controlled with B_{ext}. The magnetic MFM tip has previously been shown to be a powerful tool to manipulate domains, including

https://doi.org/10.1021/acs.nanolett.3c05058
Nano Lett. 2024, 24, 4393–4399

controlled writing and moving domains.[33,39−41] So we now investigate the possibility of using the stray field from the tip, B_{tip}, to locally manipulate the domains in the MST. To reduce the influence of B_{tip} on the sample, the domain imaging discussed so far was done with the tip lifted high (roughly 200−230 nm) above the MST surface. However, when B_{ext} is near the coercive field, small changes in the magnetic field can have a large influence on the sample magnetization, and even 200 nm from the tip, B_{tip} could be on the order of 10 mT,[57] comparable to the coercive field. Correspondingly, small changes in R_{xy} and R_{xx} during MFM imaging (Figure 1b, Supporting Information SIV) demonstrate that the tip mildly influenced the sample magnetization. Moreover, tip-induced domain flips are seen in some images as domains that abruptly disappear partway through imaging. The AHE is a good sensor for small changes in magnetization.[58−60] So, to quantify the tip's influence, we applied an AC current between contacts 2 and 4 and measured the induced transverse voltage V_{13} across contacts 1 and 3 during MFM imaging. We recorded V_{13} while scanning in order to image the evolution of V_{13} with the tip motion, meaning that V_{13} was recorded during each pixel of a scan in order to generate a simultaneous V_{13} image. The MFM image in Figure 3a shows a

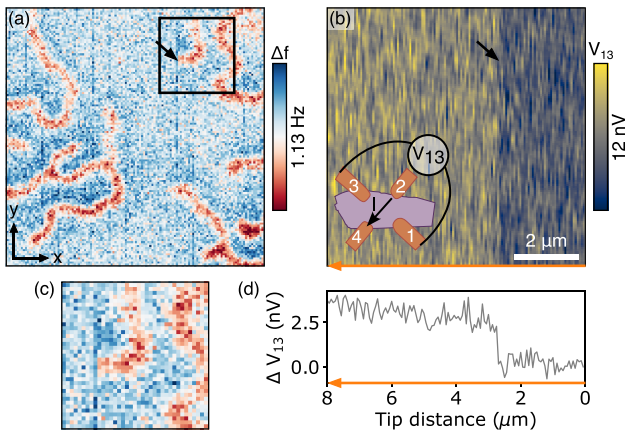

Figure 3. Impact of a single domain on transport. (a) MFM image showing a domain flipping during the scan, indicated by the black arrow. Same as Figure 1c-vi. (b) V_{13} measured simultaneously with (a), using a 500 nA amplitude AC source current. The black arrow indicates the location of the domain flip, identical with the arrow in (a). Inset: Schematic of the V_{13} measurement. (c) Zoom of (a) on the area showing the domain flip. The fast scan direction is vertical. The domain abruptly disappears from one vertical scan line to the next. (d) V_{13} averaged vertically along the fast scan direction to show the jump in value that occurred as the domain flipped. The value from the first scan line has been subtracted to show the change ΔV_{13}.

domain flip, and the simultaneously acquired V_{13} image (b,d) shows an abrupt change by more than 2 nV at the same location, demonstrating a measurable impact of the domain flip on the device transport. Interestingly the tip-induced domain flips are not always in the sense of aligning the domain with the tip, suggesting that the spatial gradient or time-dependence of B_{tip} may be equally or more important for overcoming energy barriers compared to the local Zeeman energy term.

We can harness the tip's influence to controllably write domains by bringing the tip close to the MST surface, increasing B_{tip}, similar to previous works.[33,39−41] For this purpose, we first used B_{ext} to prepare the sample with magnetization antialigned to the tip (Figure 4c). After zeroing B_{ext}, we then brought the tip into amplitude-controlled feedback on the MST surface (B_{tip} on the order of 50 mT[57]) and moved the tip across the surface to write a domain aligned with the tip. In Figure 4, we show both linear (e) and square (h) areas written with the MFM tip, demonstrating that both narrow 1D-like and 2D domains can be written. During the write process, the square area formed a mixed domain state, suggesting that, because the mixed domain state is energetically favored at $B_{ext} = 0$, there is a maximum single-domain area of roughly several μm^2 (Supporting Information SXI) that can be written. Decreasing the temperature to increase the importance of the domain wall nucleation energy may increase that area.

By inverting the magnetization of a small area locally with our MFM tip, we can directly probe that area's impact on the AHE. During domain writing, we therefore recorded V_{13} as a proxy for R_{xy} (Supporting Information SVIII). While writing the line domain, V_{13} decreased linearly (Figure 4d), matching the area scaling that one would expect for AHE contributions[44] that scale linearly with the sample average magnetization (assuming uniform thickness). V_{13} recorded while writing the square domain is also consistent with area scaling. Here, V_{13} forms two 2D images for forward (Figure 4f) and backward scans: To write the domain, the tip moved up and down along each scan line before advancing one pixel at a time left to right, so the V_{13} images display the value of V_{13} as the tip moved over each point during either the forward or backward pass. Typically, V_{13} has a finite slope on the forward pass (the blue histogram in Figure 4i is peaked at 0.6 nV/μm), confirming that the tip is writing a magnetization but not on the backward pass (orange histogram, peaked at zero). Considering that typically each scan line advances the domain wall by one pixel width (53 nm), we can quantify the local AHE: 11 nV/$(\mu m)^2$. This value is quantitatively consistent with both: (1) the linear V_{13} seen when writing the line domain and (2) the ratio of the change in V_{13} from before to after the write step to the domain area imaged via MFM (Supporting Information SXI). Moreover, the entire evolution of V_{13} during the square write can be understood in detail as a linear decrease (gray dashed line in Figure 4g) from writing the red domain plus deviations from forming the inner blue domain, in abrupt steps initially but then more smoothly near the end of the write. We provide a more detailed discussion in Supporting Information SXI.

We have therefore demonstrated a direct measurement of the scaling of the anomalous Hall effect with domain area. We note that, while previous works, e.g., refs 58 and 60−62, have also correlated domain area in a thin magnetic material with the size of the AHE, we have demonstrated that the controlled flipping of the local magnetization combined with simultaneous transport measurements directly probes the local contribution to the AHE. The technique can in principle also measure deviations from domain area scaling to probe local properties of inhomogeneous devices (spatially varying magnetization or Berry curvature). Within homogeneous materials, the area-scaling contributions and deviations represent bulk and boundary contributions, meaning that this technique can be used to probe topological effects such as dissipationless chiral edge conduction in a Chern insulator (as demonstrated by Yasuda et al.[33]) or the topological Hall effect from chiral spin textures at domain walls. We therefore emphasize the utility of controlling the relative contributions of bulk and boundary effects through the area, perimeter, and number of connected components of magnetic domains.

https://doi.org/10.1021/acs.nanolett.3c05058
Nano Lett. 2024, 24, 4393−4399

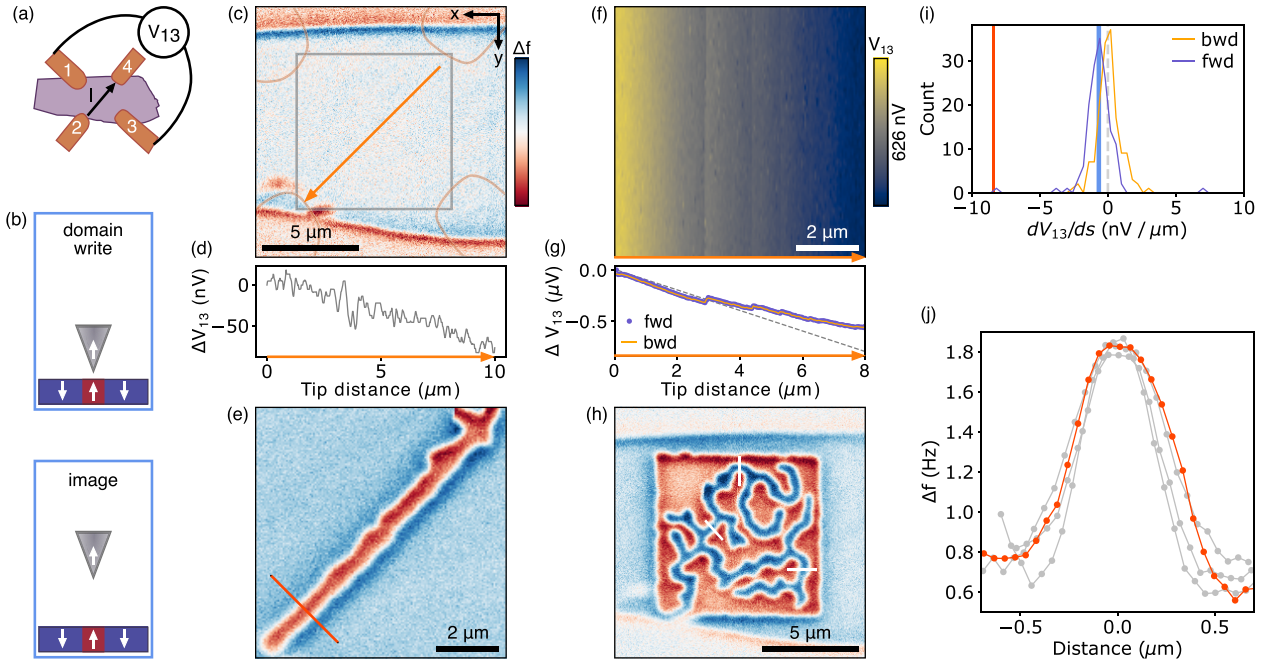

Figure 4. Writing magnetic domains. (a) Schematic of the device and the V_{13} measurement used as an approximation of the Hall response during domain writing. (b) Schematic of the magnetic tip over the MST sample during domain writing, with the tip close to the surface, and during domain imaging, with the tip lifted high above the surface. (c) MFM showing the MST device has no domains and has magnetization antialigned with the tip after ramping B_{ext} to −50 mT and then 0 mT. Constant height imaging was done with the tip lifted 300 nm above the SiO_2 surface. The overlays show the approximate locations of the electrical contacts (orange lines), the tip trajectory for writing the line domain (orange arrow), and the MFM image of the line domain (gray box). Color scale range: 1.1 Hz. (d) V_{13} measured while writing the line domain. 500 nA amplitude AC source current. (e) Constant height MFM image after writing the line domain with the tip lifted approximately 200 nm above the MST surface. The red line indicates the location of the cut shown in (j). Color scale range: 1.9 Hz. (f) V_{13} recorded as a function of the tip position while attempting to write a square area. See the main text. 500 nA amplitude AC source current. (g) V_{13} from (f) averaged vertically along the fast scan direction. The value of the first point was subtracted to show the change ΔV_{13}. The gray dashed line is the expected linear trend if the tip were fully polarizing the sample. (h) Constant height MFM image after writing the square area. Tip lifted 300 nm above the SiO_2 surface. The white lines indicate the locations of the cuts shown in (j). Color scale range: 1.6 Hz. (i) Histograms of the slopes of V_{13} during each forward and backward vertical scan line while writing the square area (f). s is the linear (1D) distance written by the tip. The vertical lines mark the slope while writing the line domain (red) and the expected per-pixel slope calculated from the overall change in V_{13} and the domain area in h (blue). (j) Line cuts through the MFM images of the line domain (red) and of the square area (gray). All cuts are offset for comparison, and the cuts from the square domain are inverted. Temperature: 10 K.

This work opens the door to making programmable magnetic devices within the ferrimagnetic compounds in the M(B,S)T family. M(B,S)T could be a platform for writable chiral currents (e.g., refs 11, 33, and 34) either in a magnetic Weyl semimetal or Chern insulating state (multiple potential band topologies have been predicted in MST[3,16,19,22,28−30]). The ability to tune magnetic domains in a compound that retains magnetic order when exfoliated to the few layer limit[1,16,32,63] raises the possibility of using M(B,S)T to introduce programmable magnetic landscapes (e.g., supperlattices or boundaries made of magnetic gradients) on length scales of hundreds of nanometers to micrometers into van der Waals heterostructures. Generically, the tip writing process allows us to locally move between different metastable magnetic configurations that are separated by energetic barriers. So beyond writing individual domains of uniform magnetization explicitly, the tip influence could be combined with external fields and temperature to stabilize and write areas of nonuniform spin textures (just as the mixed domain state formed in our square area was not uniform) in order to create functional devices based on boundaries between magnetic phases.

■ ASSOCIATED CONTENT

Supporting Information

The Supporting Information is available free of charge at https://pubs.acs.org/doi/10.1021/acs.nanolett.3c05058.

Additional experimental details, characterization of the sample topography, images of stripe domains, electrical transport measurements, analysis and modeling of domain length scales, analysis of the repeatability of bubble domain locations, analysis of the scaling of the AHE with domain area, discussion of the nature of bubble domains, and magnetization measurements of bulk MST (PDF)

■ AUTHOR INFORMATION

Corresponding Authors

Lia Krusin-Elbaum − *Department of Physics, The City College of New York, New York, New York 10027, United States*; Email: lkrusin@ccny.cuny.edu

Cory R. Dean − *Department of Physics, Columbia University, New York, New York 10027, United States*; Email: cd2478@columbia.edu

Dmitri N. Basov − *Department of Physics, Columbia University, New York, New York 10027, United States*; Email: db3056@columbia.edu

https://doi.org/10.1021/acs.nanolett.3c05058
Nano Lett. 2024, 24, 4393−4399

Abhay N. Pasupathy − *Department of Physics, Columbia University, New York, New York 10027, United States; Condensed Matter Physics and Materials Science Division, Brookhaven National Laboratory, Upton, New York 11973, United States;* orcid.org/0000-0002-2744-0634; Email: apn2108@columbia.edu

Authors

Tatiana A. Webb − *Department of Physics, Columbia University, New York, New York 10027, United States;* orcid.org/0000-0001-5694-2863

Afrin N. Tamanna − *Department of Physics, The City College of New York, New York, New York 10027, United States*

Xiaxin Ding − *Department of Physics, The City College of New York, New York, New York 10027, United States*

Nishchhal Verma − *Department of Physics, Columbia University, New York, New York 10027, United States*

Jikai Xu − *Department of Physics, Columbia University, New York, New York 10027, United States;* orcid.org/0009-0009-9535-8403

Complete contact information is available at: https://pubs.acs.org/10.1021/acs.nanolett.3c05058

Notes

The authors declare no competing financial interest.

■ ACKNOWLEDGMENTS

We thank Zachariah Addison for helpful discussions. This work was supported by the Air Force Office of Scientific Research via grant FA9550-21-1-0378 (T.A.W., A.N.P.) and by NSF grants DMR-2210186 (D.N.B) and HRD-2112550 (L.K.-E.). Research on topological properties of moiré superlattices is supported as part of Programmable Quantum Materials, an Energy Frontier Research Center funded by the U.S. Department of Energy (DOE), Office of Science, Basic Energy Sciences (BES), under award DE-SC0019443. Sample synthesis is supported by the NSF MRSEC program through Columbia University in the Center for Precision-Assembled Quantum Materials under award number DMR-2011738.

■ REFERENCES

(1) Deng, Y.; Yu, Y.; Shi, M. Z.; Guo, Z.; Xu, Z.; Wang, J.; Chen, X. H.; Zhang, Y. Quantum anomalous Hall effect in intrinsic magnetic topological insulator $MnBi_2Te_4$. *Science* **2020**, *367*, 895−900.

(2) Otrokov, M. M.; et al. Prediction and observation of an antiferromagnetic topological insulator. *Nature* **2019**, *576*, 416−422.

(3) Zhang, D.; Shi, M.; Zhu, T.; Xing, D.; Zhang, H.; Wang, J. Topological Axion States in the Magnetic Insulator $MnBi_2Te_4$ with the Quantized Magnetoelectric Effect. *Phys. Rev. Lett.* **2019**, *122*, 206401.

(4) Lei, C.; Chen, S.; MacDonald, A. H. Magnetized topological insulator multilayers. *Proc. Natl. Acad. Sci.* **2020**, *117*, 27224−27230.

(5) Deng, H.; Chen, Z.; Wołoś, A.; Konczykowski, M.; Sobczak, K.; Sitnicka, J.; Fedorchenko, I. V.; Borysiuk, J.; Heider, T.; Pluciński, Ł.; Park, K.; Georgescu, A. B.; Cano, J.; Krusin-Elbaum, L. High-temperature quantum anomalous Hall regime in a $MnBi_2Te_4/Bi_2Te_3$ superlattice. *Nat. Phys.* **2021**, *17*, 36−42.

(6) Lachman, E. O.; Young, A. F.; Richardella, A.; Cuppens, J.; Naren, H. R.; Anahory, Y.; Meltzer, A. Y.; Kandala, A.; Kempinger, S.; Myasoedov, Y.; Huber, M. E.; Samarth, N.; Zeldov, E. Visualization of superparamagnetic dynamics in magnetic topological insulators. *Sci. Adv.* **2015**, *1*, e1500740.

(7) Lee, I.; Kim, C. K.; Lee, J.; Billinge, S. J. L.; Zhong, R.; Schneeloch, J. A.; Liu, T.; Valla, T.; Tranquada, J. M.; Gu, G.; Davis, J. C. S. Imaging Dirac-mass disorder from magnetic dopant atoms in the ferromagnetic topological insulator $Cr_x(Bi_{0.1}Sb_{0.9})_{2-x}Te_3$. *Proc. Natl. Acad. Sci.* **2015**, *112*, 1316−1321.

(8) Huang, Z.; Du, M.-H.; Yan, J.; Wu, W. Native defects in antiferromagnetic topological insulator $MnBi_2Te_4$. *Phys. Rev. Mater.* **2020**, *4*, 121202.

(9) Liu, M.; Lei, C.; Kim, H.; Li, Y.; Frammolino, L.; Yan, J.; Macdonald, A. H.; Shih, C.-K. Visualizing the interplay of Dirac mass gap and magnetism at nanoscale in intrinsic magnetic topological insulators. *Proc. Natl. Acad. Sci.* **2022**, *119*, e2207681119.

(10) Liu, C.; Wang, Y.; Li, H.; Wu, Y.; Li, Y.; Li, J.; He, K.; Xu, Y.; Zhang, J.; Wang, Y. Robust axion insulator and Chern insulator phases in a two-dimensional antiferromagnetic topological insulator. *Nat. Mater.* **2020**, *19*, 522−527.

(11) Ovchinnikov, D.; Cai, J.; Lin, Z.; Fei, Z.; Liu, Z.; Cui, Y.-T.; Cobden, D. H.; Chu, J.-H.; Chang, C.-Z.; Xiao, D.; Yan, J.; Xu, X. Topological current divider in a Chern insulator junction. *Nat. Commun.* **2022**, *13*, 5967.

(12) Cai, J.; Ovchinnikov, D.; Fei, Z.; He, M.; Song, T.; Lin, Z.; Wang, C.; Cobden, D.; Chu, J.-H.; Cui, Y.-T.; Chang, C.-Z.; Xiao, D.; Yan, J.; Xu, X. Electric control of a canted-antiferromagnetic Chern insulator. *Nat. Commun.* **2022**, *13*, 1668.

(13) Eremeev, S. V.; Otrokov, M. M.; Chulkov, E. V. Competing rhombohedral and monoclinic crystal structures in $MnPn_2Ch_4$ compounds: An ab-initio study. *J. Alloys Compd.* **2017**, *709*, 172−178.

(14) Li, H.; et al. Dirac Surface States in Intrinsic Magnetic Topological Insulators $EuSn_2As_2$ and $MnBi_{2n}Te_{3n+1}$. *Phys. Rev. X* **2019**, *9*, No. 041039.

(15) Shi, M. Z.; Lei, B.; Zhu, C. S.; Ma, D. H.; Cui, J. H.; Sun, Z. L.; Ying, J. J.; Chen, X. H. Magnetic and transport properties in the magnetic topological insulators $MnB_2Te_4(Bi_2Te_3)_n$ (n = 1,2). *Phys. Rev. B* **2019**, *100*, 155144.

(16) Chen, B.; et al. Intrinsic magnetic topological insulator phases in the Sb doped $MnBi_2Te_4$ bulks and thin flakes. *Nat. Commun.* **2019**, *10*, 4469.

(17) Yan, J. Q.; Okamoto, S.; McGuire, M. A.; May, A. F.; McQueeney, R. J.; Sales, B. C. Evolution of structural, magnetic, and transport properties in $MnBi_{2-x}Sb_xTe_4$. *Phys. Rev. B* **2019**, *100*, 104409.

(18) Rienks, E. D. L.; et al. Large magnetic gap at the Dirac point in $Bi_2Te_3/MnBi_2Te_4$ heterostructures. *Nature* **2019**, *576*, 423−428.

(19) Murakami, T.; Nambu, Y.; Koretsune, T.; Xiangyu, G.; Yamamoto, T.; Brown, C. M.; Kageyama, H. Realization of interlayer ferromagnetic interaction in $MnSb_2Te_4$ toward the magnetic Weyl semimetal state. *Phys. Rev. B* **2019**, *100*, 195103.

(20) Hu, C.; et al. Realization of an intrinsic ferromagnetic topological state in $MnBi_8Te_{13}$. *Sci. Adv.* **2020**, *6*, eaba4275.

(21) Riberolles, S. X. M.; Zhang, Q.; Gordon, E.; Butch, N. P.; Ke, L.; Yan, J. Q.; McQueeney, R. J. Evolution of magnetic interactions in Sb-substituted $MnBi_2Te_4$. *Phys. Rev. B* **2021**, *104*, No. 064401.

(22) Ma, X.-M.; et al. Realization of a tunable surface Dirac gap in Sb-doped $MnBi_2Te_4$. *Phys. Rev. B* **2021**, *103*, L121112.

(23) Lai, Y.; Ke, L.; Yan, J.; McDonald, R. D.; McQueeney, R. J. Defect-driven ferrimagnetism and hidden magnetization in $MnBi_2Te_4$. *Phys. Rev. B* **2021**, *103*, 184429.

(24) Liu, Y.; Wang, L. L.; Zheng, Q.; Huang, Z.; Wang, X.; Chi, M.; Wu, Y.; Chakoumakos, B. C.; McGuire, M. A.; Sales, B. C.; Wu, W.; Yan, J. Site Mixing for Engineering Magnetic Topological Insulators. *Phys. Rev. X* **2021**, *11*, No. 021033.

(25) Ge, W.; Sass, P. M.; Yan, J.; Lee, S. H.; Mao, Z.; Wu, W. Direct evidence of ferromagnetism in $MnSb_2Te_4$. *Phys. Rev. B* **2021**, *103*, 134403.

(26) Hayami, S.; Lin, S.-Z.; Batista, C. D. Bubble and skyrmion crystals in frustrated magnets with easy-axis anisotropy. *Phys. Rev. B* **2016**, *93*, 184413.

(27) Li, B.; Yan, J. Q.; Pajerowski, D. M.; Gordon, E.; Nedić, A. M.; Sizyuk, Y.; Ke, L.; Orth, P. P.; Vaknin, D.; McQueeney, R. J. Competing Magnetic Interactions in the Antiferromagnetic Topological Insulator $MnBi_2Te_4$. *Phys. Rev. Lett.* **2020**, *124*, 167204.

(28) Zhou, L.; Tan, Z.; Yan, D.; Fang, Z.; Shi, Y.; Weng, H. Topological phase transition in the layered magnetic compound $MnSb_2Te_4$: Spin-orbit coupling and interlayer coupling dependence. *Phys. Rev. B* **2020**, *102*, No. 085114.
(29) Wimmer, S.; et al. Mn-Rich $MnSb_2Te_4$: A Topological Insulator with Magnetic Gap Closing at High Curie Temperatures of 45−50 K. *Adv. Mater.* **2021**, *33*, 2102935.
(30) Tamanna, A. N.; Lakra, A.; Ding, X.; Buzi, E.; Park, K.; Sobczak, K.; Deng, H.; Sharma, G.; Tewari, S.; Krusin-Elbaum, L. Hydrogen induces chiral conduction channels in the topological magnet. *arXiv* (cond-mat); 2023. DOI: 10.48550/arXiv.2312.02315 (accessed December 17, 2023).
(31) Li, J.; Wang, C.; Zhang, Z.; Gu, B.-L.; Duan, W.; Xu, Y. Magnetically controllable topological quantum phase transitions in the antiferromagnetic topological insulator $MnBi_2Te_4$. *Phys. Rev. B* **2019**, *100*, 121103.
(32) Ovchinnikov, D.; et al. Intertwined Topological and Magnetic Orders in Atomically Thin Chern Insulator $MnBi_2Te_4$. *Nano Lett.* **2021**, *21*, 2544−2550.
(33) Yasuda, K.; Mogi, M.; Yoshimi, R.; Tsukazaki, A.; Takahashi, K. S.; Kawasaki, M.; Kagawa, F.; Tokura, Y. Quantized chiral edge conduction on domain walls of a magnetic topological insulator. *Science* **2017**, *358*, 1311−1314.
(34) Rosen, I. T.; Fox, E. J.; Kou, X.; Pan, L.; Wang, K. L.; Goldhaber-Gordon, D. Chiral transport along magnetic domain walls in the quantum anomalous Hall effect. *npj Quantum Mater.* **2017**, *2*, 69.
(35) Malozemoff, A. P.; Slonczewski, J. C. *Magnetic Domain Walls in Bubble Materials*; Elsevier: 1979.
(36) O'Dell, T. H. Magnetic bubble domain devices. *Rep. Prog. Phys.* **1986**, *49*, 589−620.
(37) Parkin, S. S. P.; Hayashi, M.; Thomas, L. Magnetic Domain-Wall Racetrack Memory. *Science* **2008**, *320*, 190−194.
(38) Woo, S.; et al. Observation of room-temperature magnetic skyrmions and their current-driven dynamics in ultrathin metallic ferromagnets. *Nat. Mater.* **2016**, *15*, 501−506.
(39) Zhang, S.; Zhang, J.; Zhang, Q.; Barton, C.; Neu, V.; Zhao, Y.; Hou, Z.; Wen, Y.; Gong, C.; Kazakova, O.; Wang, W.; Peng, Y.; Garanin, D. A.; Chudnovsky, E. M.; Zhang, X. Direct writing of room temperature and zero field skyrmion lattices by a scanning local magnetic field. *Appl. Phys. Lett.* **2018**, *112*, 132405.
(40) Temiryazev, A. G.; Temiryazeva, M. P.; Zdoroveyshchev, A. V.; Vikhrova, O. V.; Dorokhin, M. V.; Demina, P. B.; Kudrin, A. V. Formation of a Domain Structure in Multilayer CoPt Films by Magnetic Probe of an Atomic Force Microscope. *Phys. Solid State* **2018**, *60*, 2200−2206.
(41) Casiraghi, A.; Corte-León, H.; Vafaee, M.; Garcia-Sanchez, F.; Durin, G.; Pasquale, M.; Jakob, G.; Kläui, M.; Kazakova, O. Individual skyrmion manipulation by local magnetic field gradients. *Commun. Phys.* **2019**, *2*, 145.
(42) Schwarz, A.; Wiesendanger, R. Magnetic sensitive force microscopy. *Nano Today* **2008**, *3*, 28−39.
(43) Hartmann, U. Magnetic Force Microscopy. *Annu. Rev. Mater. Sci.* **1999**, *29*, 53−87.
(44) Nagaosa, N.; Sinova, J.; Onoda, S.; MacDonald, A. H.; Ong, N. P. Anomalous Hall effect. *Rev. Mod. Phys.* **2010**, *82*, 1539−1592.
(45) Giess, E. A. Magnetic Bubble Materials. *Science* **1980**, *208*, 938−943.
(46) Seul, M.; Andelman, D. Domain Shapes and Patterns: The Phenomenology of Modulated Phases. *Science* **1995**, *267*, 476−483.
(47) Liebmann, M.; Schwarz, A.; Kaiser, U.; Wiesendanger, R.; Kim, D. W.; Noh, T. W. Magnetization reversal of a structurally disordered Manganite thin film with perpendicular anisotropy. *Phys. Rev. B* **2005**, *71*, 104431.
(48) Davies, J. E.; Hellwig, O.; Fullerton, E. E.; Denbeaux, G.; Kortright, J. B.; Liu, K. Magnetization reversal of Co/Pt multilayers: Microscopic origin of high-field magnetic irreversibility. *Phys. Rev. B* **2004**, *70*, 224434.
(49) Hubert, A.; Schäfer, R. *Magnetic Domains*; Springer: Berlin, Heidelberg, 1998.
(50) Soumyanarayanan, A.; Raju, M.; Gonzalez Oyarce, A. L.; Tan, A. K. C.; Im, M.-Y.; Petrovic, A. P.; Ho, P.; Khoo, K. H.; Tran, M.; Gan, C. K.; Ernult, F.; Panagopoulos, C. Tunable room-temperature magnetic skyrmions in Ir/Fe/Co/Pt multilayers. *Nat. Mater.* **2017**, *16*, 898−904.
(51) Ding, B.; Li, Z.; Xu, G.; Li, H.; Hou, Z.; Liu, E.; Xi, X.; Xu, F.; Yao, Y.; Wang, W. Observation of Magnetic Skyrmion Bubbles in a van der Waals Ferromagnet Fe_3GeTe_2. *Nano Lett.* **2020**, *20*, 868−873.
(52) Chakraborty, A.; Srivastava, A. K.; Sharma, A. K.; Gopi, A. K.; Mohseni, K.; Ernst, A.; Deniz, H.; Hazra, B. K.; Das, S.; Sessi, P.; Kostanovskiy, I.; Ma, T.; Meyerheim, H. L.; Parkin, S. S. P. Magnetic Skyrmions in a Thickness Tunable 2D Ferromagnet from a Defect Driven Dzyaloshinskii−Moriya Interaction. *Adv. Mater.* **2022**, *34*, 2108637.
(53) Park, T.-E.; et al. Néel-type skyrmions and their current-induced motion in van der Waals ferromagnet-based heterostructures. *Phys. Rev. B* **2021**, *103*, 104410.
(54) Sharma, A. K.; Jena, J.; Rana, K. G.; Markou, A.; Meyerheim, H. L.; Mohseni, K.; Srivastava, A. K.; Kostanoskiy, I.; Felser, C.; Parkin, S. S. P. Nanoscale Noncollinear Spin Textures in Thin Films of a D_{2d} Heusler Compound. *Adv. Mater.* **2021**, *33*, 2101323.
(55) Wang, W.; Zhao, Y.-F.; Wang, F.; Daniels, M. W.; Chang, C.-Z.; Zang, J.; Xiao, D.; Wu, W. Chiral-Bubble-Induced Topological Hall Effect in Ferromagnetic Topological Insulator Heterostructures. *Nano Lett.* **2021**, *21*, 1108−1114.
(56) Montoya, S. A.; Couture, S.; Chess, J. J.; Lee, J. C. T.; Kent, N.; Henze, D.; Sinha, S. K.; Im, M.-Y.; Kevan, S. D.; Fischer, P.; McMorran, B. J.; Lomakin, V.; Roy, S.; Fullerton, E. E. Tailoring magnetic energies to form dipole skyrmions and skyrmion lattices. *Phys. Rev. B* **2017**, *95*, No. 024415.
(57) Rizzo, D. J.; McLeod, A. S.; Carnahan, C.; Telford, E. J.; Dismukes, A. H.; Wiscons, R. A.; Dong, Y.; Nuckolls, C.; Dean, C. R.; Pasupathy, A. N.; Roy, X.; Xiao, D.; Basov, D. N. Visualizing Atomically Layered Magnetism in CrSBr. *Adv. Mater.* **2022**, *34*, 2201000.
(58) Kikuchi, N.; Okamoto, S.; Kitakami, O.; Shimada, Y.; Fukamichi, K. Sensitive detection of irreversible switching in a single FePt nanosized dot. *Appl. Phys. Lett.* **2003**, *82*, 4313−4315.
(59) Cornelissens, Y. G.; Peeters, F. M. Response function of a Hall magnetosensor in the diffusive regime. *J. Appl. Phys.* **2002**, *92*, 2006−2012.
(60) Delalande, M.; de Vries, J.; Abelmann, L.; Lodder, J. C. Measurement of the nucleation and domain depinning field in a single Co/Pt multilayer dot by Anomalous Hall effect. *J. Magn. Magn. Mater.* **2012**, *324*, 1277−1280.
(61) Schwarz, A.; Liebmann, M.; Kaiser, U.; Wiesendanger, R.; Noh, T. W.; Kim, D. W. Visualization of the Barkhausen Effect by Magnetic Force Microscopy. *Phys. Rev. Lett.* **2004**, *92*, No. 077206.
(62) Maccariello, D.; Legrand, W.; Reyren, N.; Garcia, K.; Bouzehouane, K.; Collin, S.; Cros, V.; Fert, A. Electrical detection of single magnetic skyrmions in metallic multilayers at room temperature. *Nat. Nanotechnol.* **2018**, *13*, 233−237.
(63) Zang, Z.; et al. Layer-Number-Dependent Antiferromagnetic and Ferromagnetic Behavior in $MnSb_2Te_4$. *Phys. Rev. Lett.* **2022**, *128*, No. 017201.

https://doi.org/10.1021/acs.nanolett.3c05058
Nano Lett. 2024, 24, 4393−4399